# *Supplementary Materials for*

# "Induced gravitational effect and stress change by tsunami surge"

Byeongwoo Kim[1], Tae-Kyung Hong[1*], Junhyung Lee[1],

Seongjun Park[1], and Jeongin Lee[1]

## Affiliation and address:

[1]Yonsei University, Department of Earth System Sciences, 50 Yonsei-ro, Seodaemun-gu Seoul 03722, South Korea.

## Correspondence to:

tkhong@yonsei.ac.kr (Tae-Kyung Hong)

## Contents of this file



## Introduction

The supplementary materials provide additional information and figures.

## Earthquake and tsunami observations

The 1 January 2024 $M_W$ 7.5 earthquake occurred in the northern Noto Peninsula (Fig. S1). A tsunami was produced by the earthquake, arriving at the east coast of the Korean Peninsula. Seismic waves from the earthquake were recorded at densely-deployed seismic stations in the Korean Peninsula and ocean-bottom seismometers off the Korean Peninsula (Fig. S1). The tsunami waves are well observed in tide gauges off the east coast of the Korean Peninsula (Fig. S2).

Seismic waves from the earthquake arrive $<$ 20 minutes (Fig. S3). The direct seismic waves are observed at most seismic stations in the Korean Peninsula and detected in the frequency range of 0.003-2 Hz (more apparently in 0.03-0.1 Hz). After the direct seismic waves, long-period tsunami-induced seismic signals are observed more than 48 hours (Fig. S4). The tsunami-induced seismic signals are observed in low frequencies of 0.0002-0.2 Hz (more apparently in 0.0003-0.01 Hz) at seismic stations on the east coast of the Korean Peninsula.

We determine the phase polarization directions using an eigenvector analysis that is applied to 40-s-long waveforms bandpass-filtered between 0.03 and 0.1 Hz (Fig. S5). *P* and Rayleigh waves are polarized in the great-circle directions between the earthquake and stations (radial directions). *SH* phases are polarized in the tangential directions. The seismic wavetrains are mixed with phases polarized in radial or tangential directions (Fig. S5).

Tsunami-induced seismic signals appear after the major seismic phases for more than 60 hours. We also determine the polarization directions of tsunami-induced seismic signals

that are bandpass-filtered between 0.0005 and 0.0011 Hz (Fig. S6). The narrow frequency band confines the tsunami-induced seismic signals effectively, allowing us to measure the polarization directions accurately. The polarization directions of tsunami-induced seismic signals are apparently different from those of seismic phases from the earthquake. The tsunami-induced seismic signals are horizontally polarized. The polarization directions of tsunami-induced seismic signals are dependent on the locations of stations (Fig. S7). The polarization directions of tsunami-induced signals are nearly perpendicular to the coastline adjacent to the stations.

The spectral contents of tsunami-induced seismic signals are compared with those of tsunami records in adjacent tide gauges (Fig. S8). The tsunami waves in tide gauges are strong at frequencies of 0.0001-0.0015 Hz (Fig. S9). On the other hand, the wavetrains with tsunami-induced seismic signals are strong in frequencies of 0.0002-0.2 Hz with peak energy around 0.001 Hz (Fig. S9). The spectral contents of tsunami-induced seismic signals are distinguished from those of tsunami waves, seismic waves and ambient noise (Fig. S9).

The frequency contents of tsunami-induced signals are similar to those of tsunami records, presenting energy distribution in 0.001-0.008 Hz. However, the dominant frequencies are slightly higher in the tsunami records (Fig. S9). Also, reflected body waves and surface waves traveling around the Earth appear in high frequencies ($>$ 0.002 Hz), interfering with the tsunami-induced seismic signals (Fig. S10).

## Amplitude relationship

The tsunami waves are coupled with seismic signals due to tidal loading on the coast. We determine the relationship between the amplitude of tsunami-induced seismic signals in seismometers and those of tsunami waves in tide gauges. From the constant amplitude ratios between seismic-induced seismic signals and tsunami waves, we find a linear relationship:

$$A_S^0 = C_1 A_T + C_2, \tag{1}$$

where $A_T$ is the amplitude of tsunami wave, $A_S^0$ is the amplitude of tsunami-induced seismic signal at the coast, and $C_1$ and $C_2$ are constants. The tsunami-induced seismic signals may be similar to plane waves from a line source, decaying with the square root of distance ($\sqrt{d}$).

The tsunami-induced ground motions are dominant in the Earth surface that are influenced by near surface medium properties. The near surface site effect is controlled by the average shear wave velocity within the upper 30 m depth ($V_{S30}$). The seismic amplification factor $F$ for site effect is given by (Borcherdt, 1994; Boore and Atkinson, 2008; Boore et al., 2014; Stewart et al., 2020; Aaqib et al., 2021)

$$F = \left(\frac{V_{ref}}{V_{S30}}\right)^n, \tag{2}$$

where $V_{ref}$ is the reference $V_{S30}$ value, and $n$ is a constant factor. The amplification factor is frequency dependent, decaying generally with decreasing frequency at $< 0.2$ Hz (Choi and Stewart, 2005; Boore and Atkinson, 2008; Laurendeau et al., 2013; Seyhan and Stewart, 2014; Stewart et al., 2020).

We, thus, have the amplitude of horizontal (AR) tsunami-induced seismic signal at distance $d$ (m) from the coast ($A_S$) to be

$$\begin{aligned} A_S &= E_1 \frac{\sqrt{d_{ref}}}{\sqrt{d}} \left(\frac{V_{ref}}{V_{S30}}\right)^n A_T + E_2, \\ &= E_1 A_T^* + E_2, \end{aligned} \tag{3}$$

where $E_1$ and $E_2$ are constants, $d_{ref}$ is the reference distance, and $A_T^*$ is the converted tsunami amplitude modulated by distance ($d$) and site effect ($V_{S30}$). We use the $V_{S30}$ values at the seismic stations from a national $V_{S30}$ model (Kim and Hong, 2022). Also, we set $V_{ref}$ to be 760 m/s, $d_{ref}$ to be 1 m, and $n$ to be 0.7 (Choi and Stewart, 2005; Boore and Atkinson, 2008; Boore et al., 2014; Stewart et al., 2020).

We find a linear relationship between the amplitudes of tsunami-induced seismic signals and converted tsunami amplitude ($A_T^*$):

$$A_S = 1.08 A_T^* - 6.46. \tag{4}$$

## Dynamic stress change and seismicity

We estimate dynamic stress changes induced by the seismic waves and tsunami-induced seismic signals (Figs. S11, S12). In order to minimize the influence of seismic phases from the earthquake, we analyze the wavetrains in 3-8 hours after the event origin time. The velocity wavetrains are bandpass filtered between 0.0005 and 0.0011 Hz for the analysis.

The dynamic stress change, $\sigma_m$, is assessed by (Hill and Prejean, 2007)

$$\sigma_m = \mu \frac{V_m}{\beta}, \tag{5}$$

where $\mu$ is the shear modulus, $V_m$ is the peak ground velocity (PGV), and $\beta$ is the shear wave velocity. The shear modulus is set to 34.95 GPa, and the shear wave velocity is 3.58 km/s (Chang and Baag, 2006; Jo and Hong, 2013; Hong et al., 2016, 2020; Park et al., 2021). We calculate PGV in each horizontal and vertical velocity records. The horizontal velocity records, $V_h(t)$, is computed by

$$V_h(t) = \sqrt{V_E(t)^2 + V_N(t)^2} \tag{6}$$

where $V_E(t)$ and $V_N(t)$ are the velocity records in EW and NS components, and $t$ is time.

The maximum peak dynamic stress changes induced by the seismic waves from the earthquake are 68 kPa in the horizontal direction and 39 kPa in the vertical direction (Fig. S13). The peak dynamic stress changes by the tsunami-induced seismic signals reach $\sim$ 0.81 kPa around the east coast of the Korean Peninsula (Fig. S13).

We observe some earthquakes in near offshore regions before and after the Noto Peninsula earthquake and tsunami (Fig. S14). We observe no apparent changes in focal depths after the tsunami arrival. The observation suggests that the dynamic stress changes are not enough to induce seismicity in the offshore and inland regions.

## References

Aaqib, M., Park, D., Adeel, M. B., Hashash, Y. M., and Ilhan, O. (2021). Simulation-based site amplification model for shallow bedrock sites in Korea. Earthquake Spectra, 37(3), 1900-1930.

Boore, D. M., and Atkinson, G. M. (2008). Ground-motion prediction equations for the average horizontal component of PGA, PGV, and 5%-damped PSA at spectral periods between 0.01 s and 10.0 s. Earthquake spectra, 24(1), 99-138.

Boore, D. M., Stewart, J. P., Seyhan, E., and Atkinson, G. M. (2014). NGA-West2 equations for predicting PGA, PGV, and 5% damped PSA for shallow crustal earthquakes. Earthquake Spectra, 30(3), 1057-1085.

Borcherdt, R. D. (1994). Estimates of site-dependent response spectra for design (methodology and justification). Earthquake spectra, 10(4), 617-653.

Chang, S. J., and Baag, C. E. (2006). Crustal structure in southern Korea from joint analysis of regional broadband waveforms and travel times. Bulletin of the Seismological Society of America, 96(3), 856-870.

Choi, Y., and Stewart, J. P. (2005). Nonlinear site amplification as function of 30 m shear wave velocity. Earthquake spectra, 21(1), 1-30.

Hill, D.P., and Prejean, S.G., (2007). Dynamic Triggering. In: Kanamori, H. (Ed.), Earthquake Seismology, Treatise on Geophysics Vol. volume 4. Elsevier, Amsterdam, p257-291.

Hong, T.-K., Choi, E., Park, S., and Shin, J. S. (2016). Prediction of ground motion and dynamic stress change in Baekdusan (Changbaishan) volcano caused by a North Korean nuclear explosion. Scientific reports, 6(1), 21477, doi:10.1038/srep21477.

Hong, T.-K., Park, S., Lee, J., and Kim, W. (2020). Spatiotemporal seismicity evolution and seismic hazard potentials in the western East Sea (Sea of Japan). Pure and Applied Geophysics, 177(8), 3761-3774.

Jo, E., and Hong, T.-K. (2013). Vp/Vs ratios in the upper crust of the southern Korean Peninsula and their correlations with seismic and geophysical properties. Journal of Asian Earth Sciences, 66, 204-214.

Kim, B., and Hong, T.-K. (2022). A national $V_{S30}$ model for South Korea to combine nationwide dense borehole measurements with ambient seismic noise analysis. Earth and Space Science, 9(1), e2021EA002066. https://doi.org/10.1029/2021EA002066

Laurendeau, A., Cotton, F., Ktenidou, O. J., Bonilla, L. F., and Hollender, F. (2013). Rock and stiff-soil site amplification: Dependency on $V_{S30}$ and kappa ($\kappa_0$). Bulletin of the

Seismological Society of America, 103(6), 3131-3148.

Park, S., Hong, T.-K., and Rah, G. (2021). Seismic hazard assessment for the Korean Peninsula. Bulletin of the Seismological Society of America, 111(5), 2696-2719.

Seyhan, E., and Stewart, J. P. (2014). Semi-empirical nonlinear site amplification from NGA-West2 data and simulations. Earthquake Spectra, 30(3), 1241-1256.

Stewart, J. P., Parker, G. A., Atkinson, G. M., Boore, D. M., Hashash, Y. M., and Silva, W. J. (2020). Ergodic site amplification model for central and eastern North America. Earthquake Spectra, 36(1), 42-68.

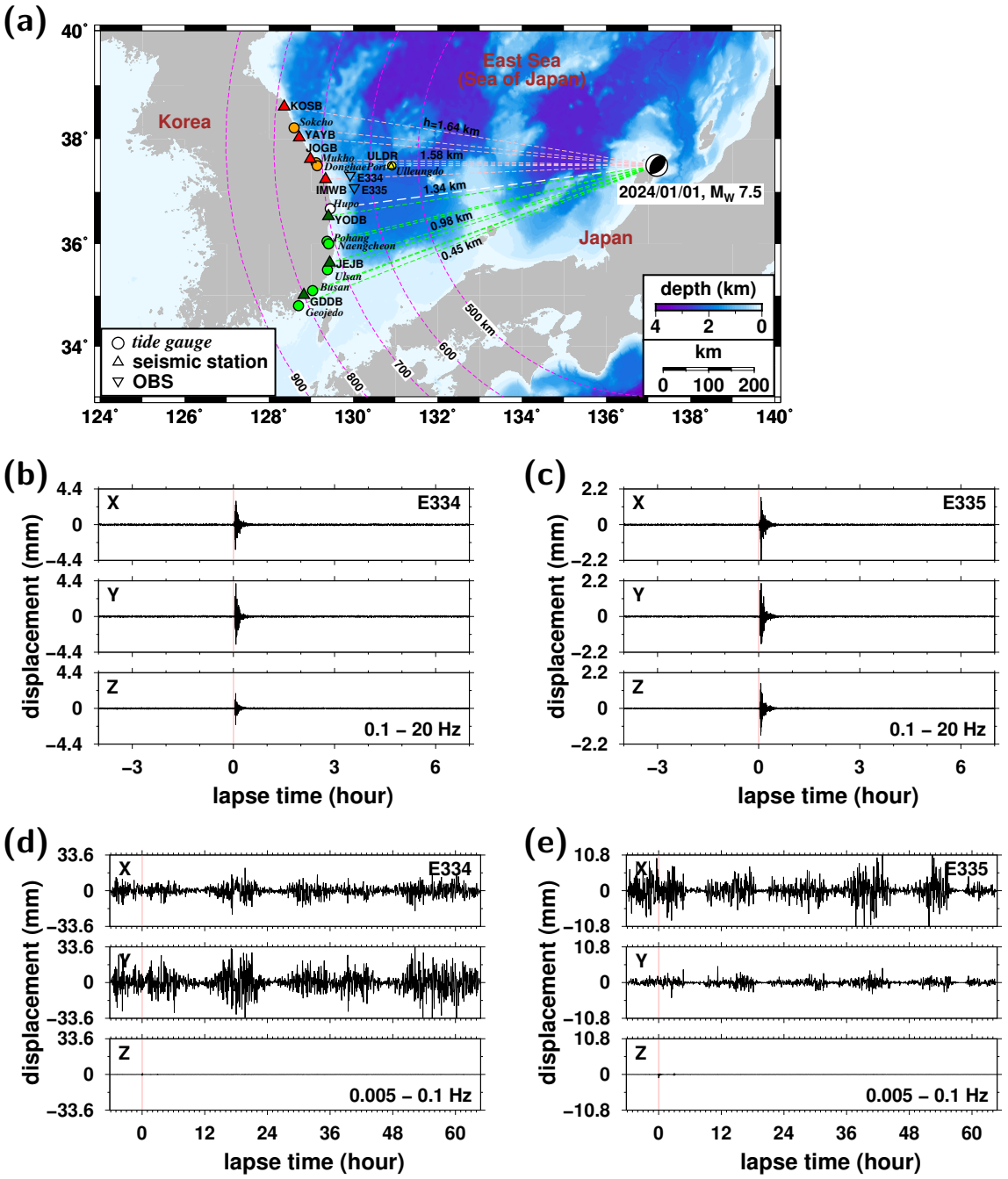


**Figure S1.** (a) Map of the 1 January 2024 $M_W$ 7.5 Noto Peninsula earthquake and seismic stations in the Korean Peninsula. Inland seismometers (circles), ocean bottom seismometers (inverted triangles), and tide gauges (triangles) are marked. Average ocean depths are presented on the paths. Seismic record sections of 0.1-20 Hz at ocean bottom seismometers (OBSs) (b) E334 and (c) E335, and those of 0.005-0.1 Hz at OBSs (d) E334 and (e) E336. Seismic waves from the earthquake are well observed in the higher frequencies. Tsunami-induced seismic signals are hardly observed.

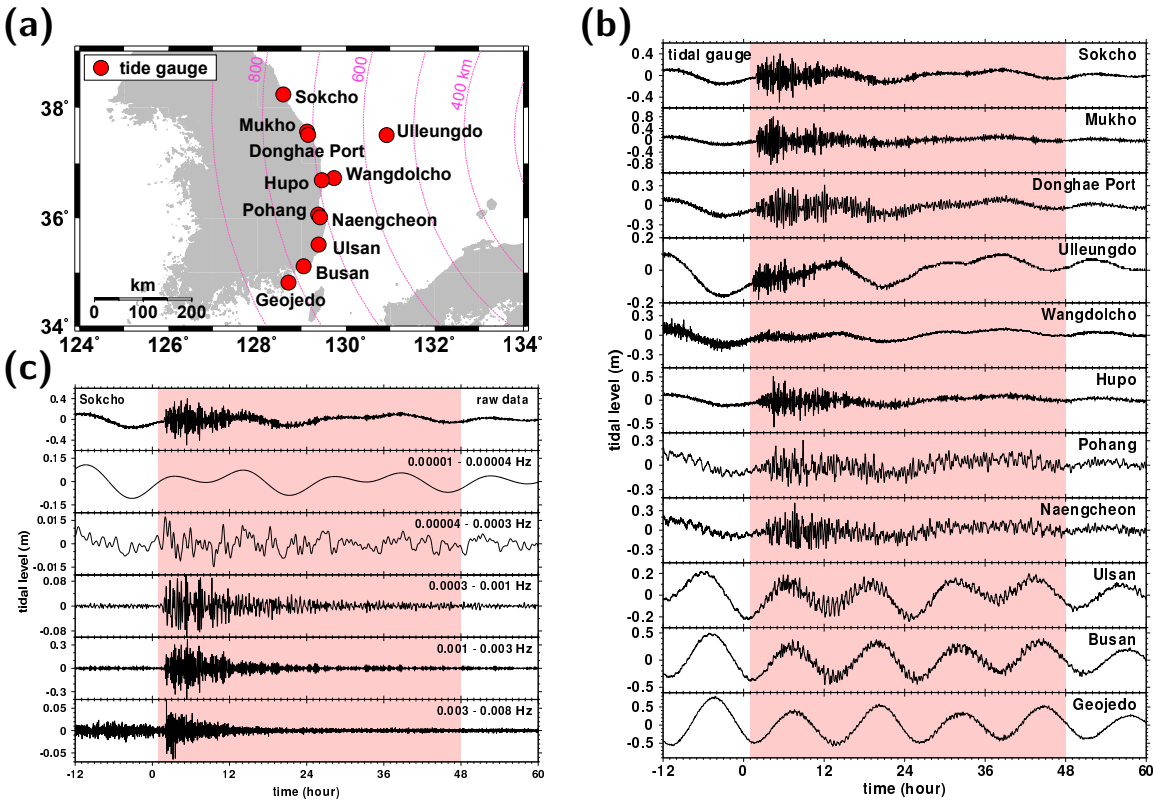


**Figure S2.** Tsunami-wave records in tide gauges: (a) map of the tide gauges, (b) raw tide records, and (c) filtered tide records. The filtering frequency bands are indicated. The tsunami arrivals are strong at the northern tide gauges, while weak at the southern tide gauges.

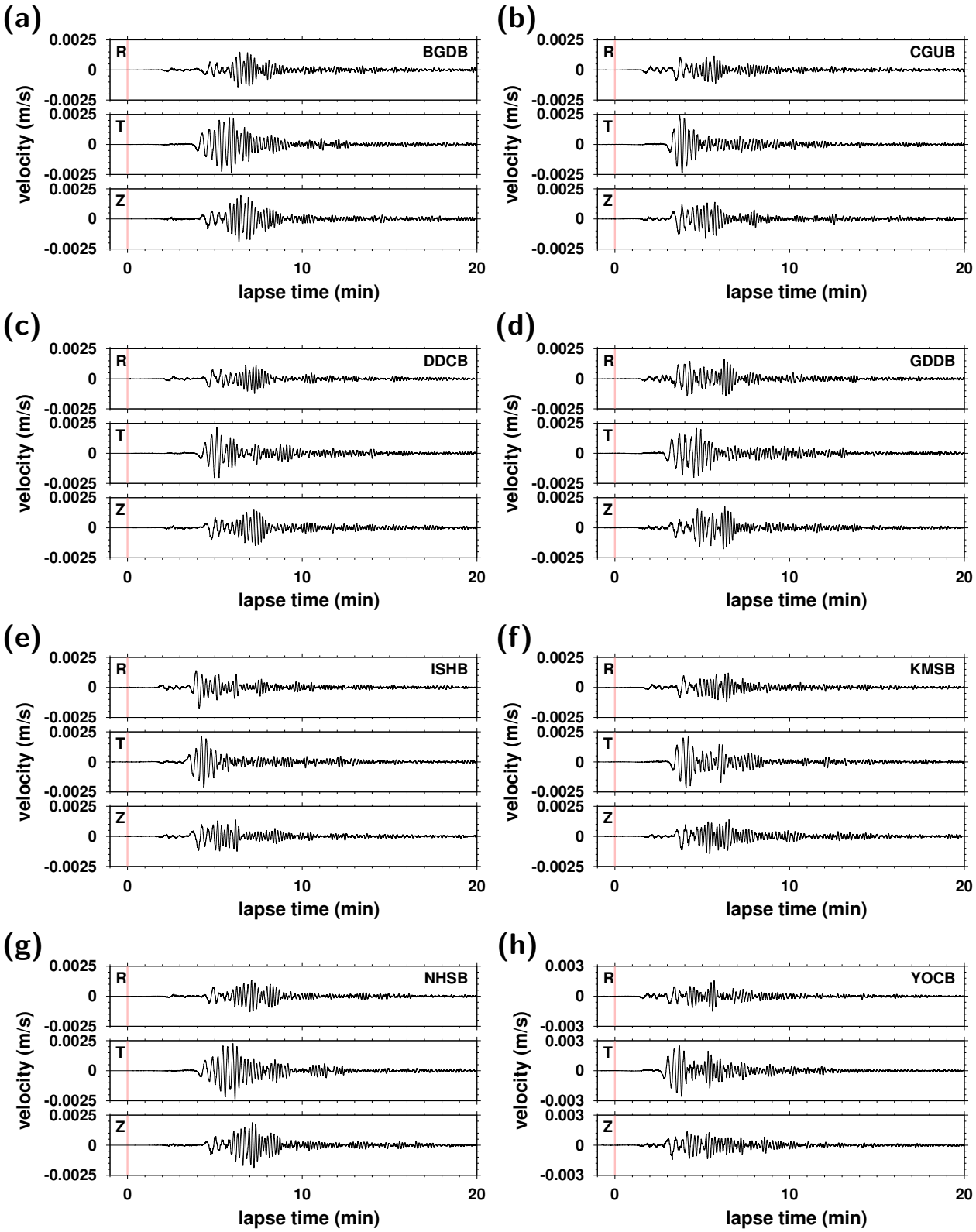


**Figure S3.** Three-component record sections of selected borehole broadband seismic stations (a) BGDB, (b) CGUB, (c) DOCB, (d) GDDB, (e) ISHB, (f) KMSB, (g) NHSB, and (h) YOCB for the seismic waves from the 1 January 2024 $M_W$ 7.5 Noto Peninsula earthquake.

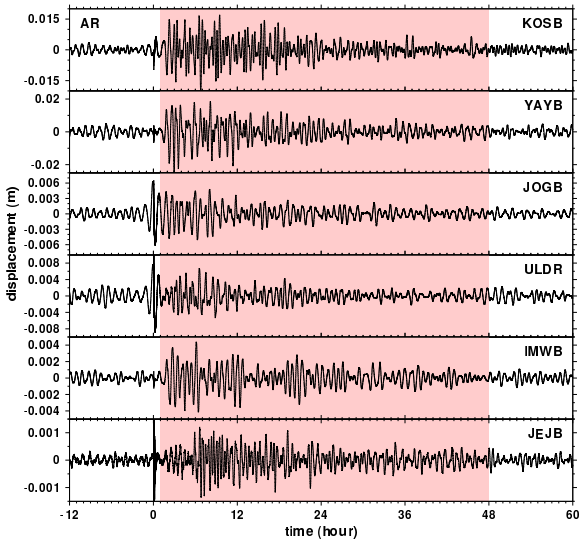


**Figure S4.** Tsunami-induced seismic signals at 0.0003-0.01 Hz recorded by seismic stations. The tsunami-induced signals are marked. The tsunami-induced signals last more than 48 hours.

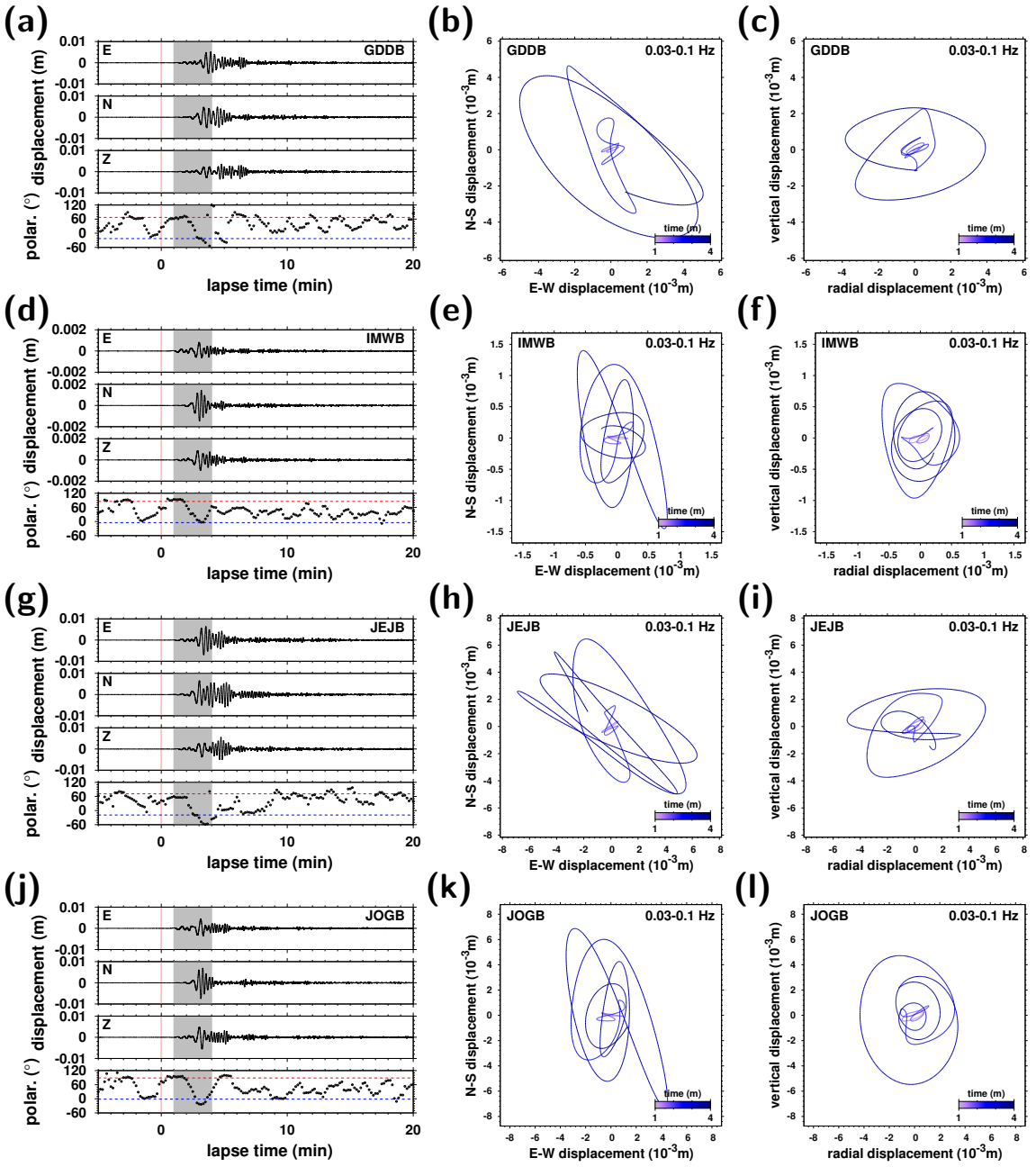


**Figure S5.** Three-component records, lateral polarization directions, and particle motions of seismic waves from the earthquake. (a) Record sections for station GDDB, and their particle motions on (b) the NS-EW plane and (c) radial-vertical plane. Same for stations (d), (e), and (f) IMWB; (g), (h), and (i) JEJB; (j), (k), (l) JOJB; (m), (n), and (o) KOSB; (p), (q), and (r) ULDR; (s), (t), and (u) YAYB; (v), (w), and (x) YODB. Great-circle directions to the event and the tangential directions are marked with dashed lines in the lateral polarization directions. Particle motions are plotted for the indicated time range (shaded time range).

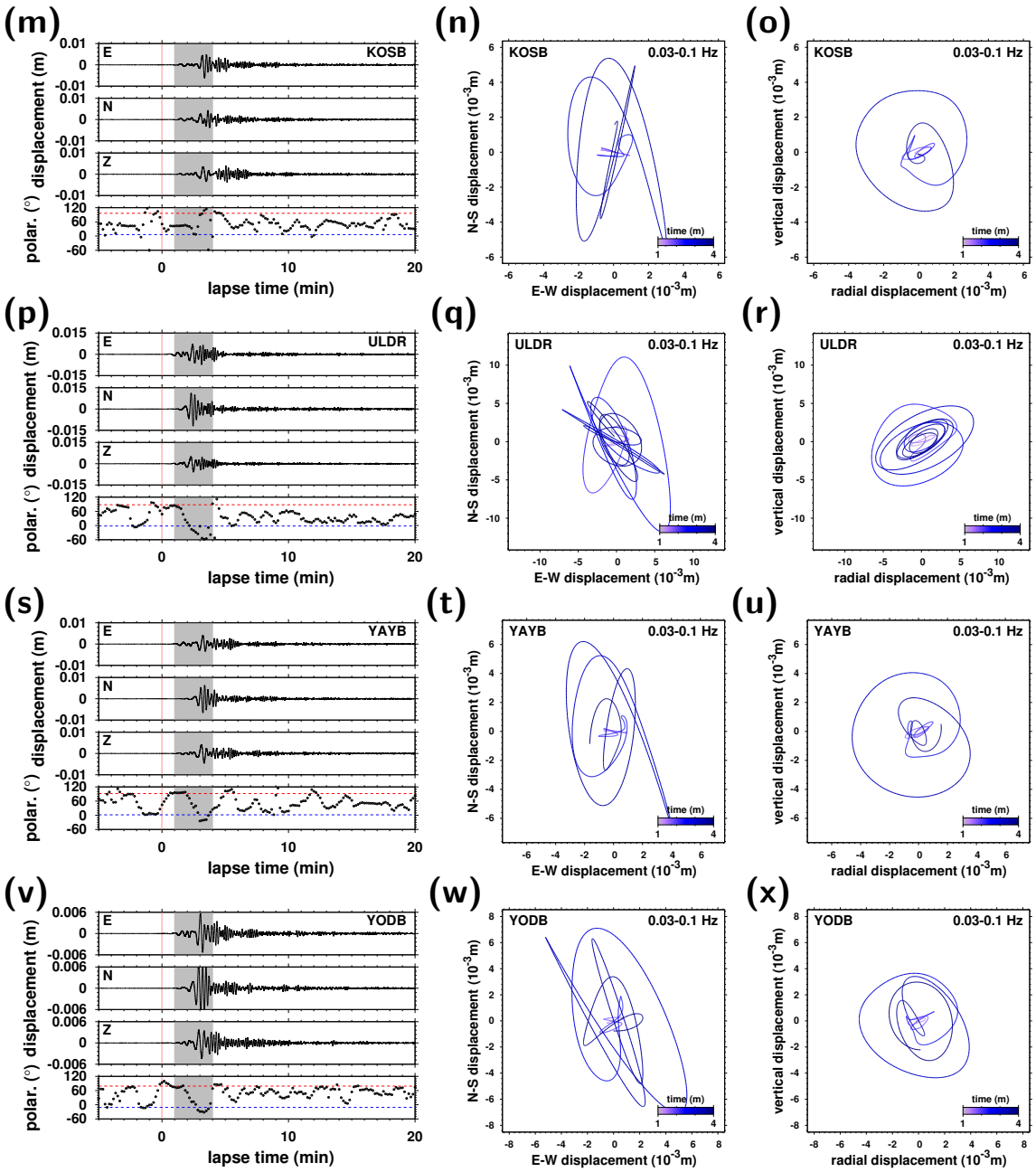


**Figure S5.** *(continued)*

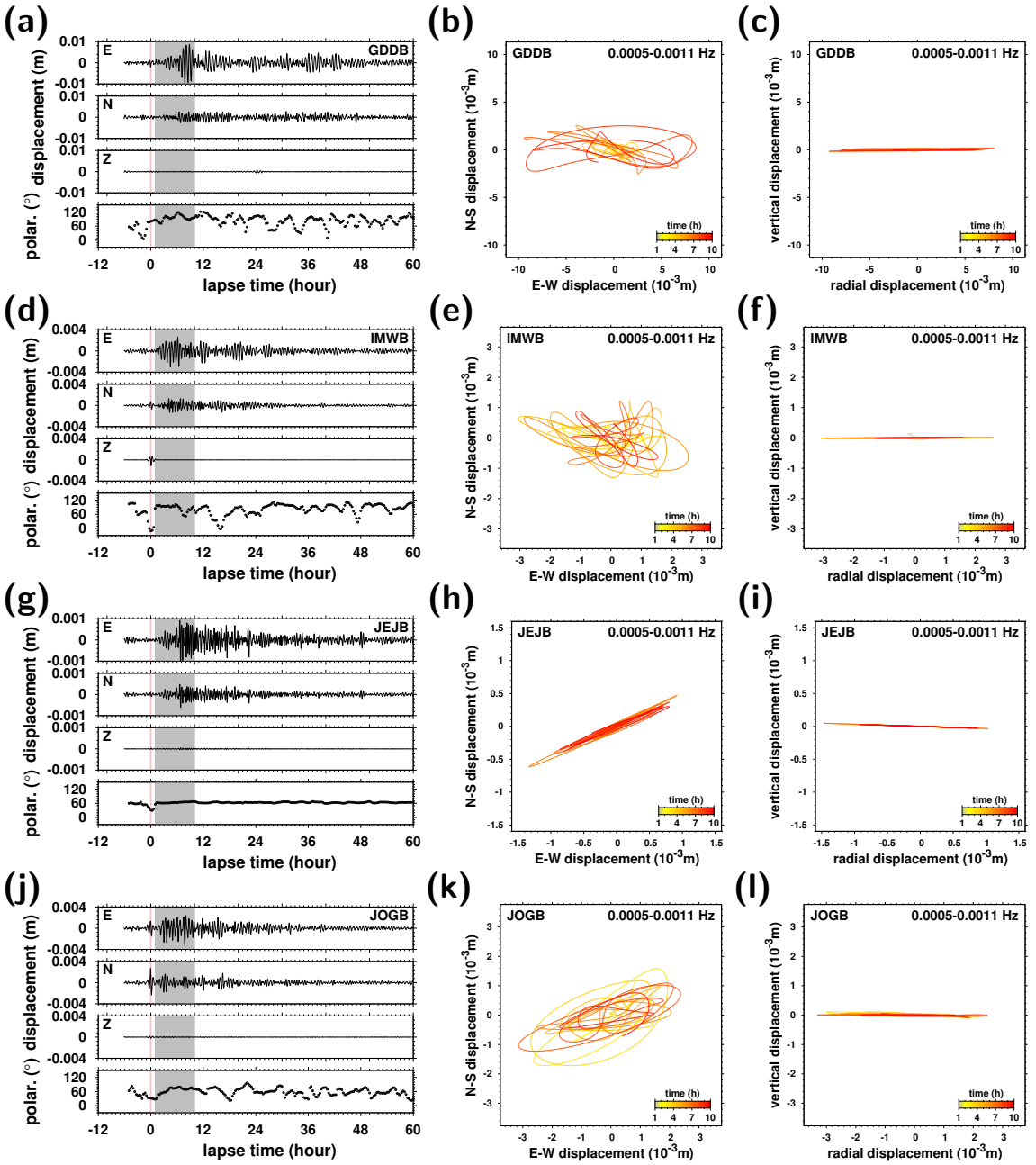


**Figure S6.** Three-component records, lateral polarization directions, and particle motions of tsunami-induced seismic signals. (a) Record sections for station GDDB, and their particle motions on (b) the NS-EW plane and (c) radial-vertical plane. Same for stations (d), (e), and (f) IMWB; (g), (h), and (i) JEJB; (j), (k), (l) JOJB; (m), (n), and (o) KOSB; (p), (q), and (r) ULDR; (s), (t), and (u) YAYB; (v), (w), and (x) YODB. Particle motions are plotted for the indicated time range (shaded time range).

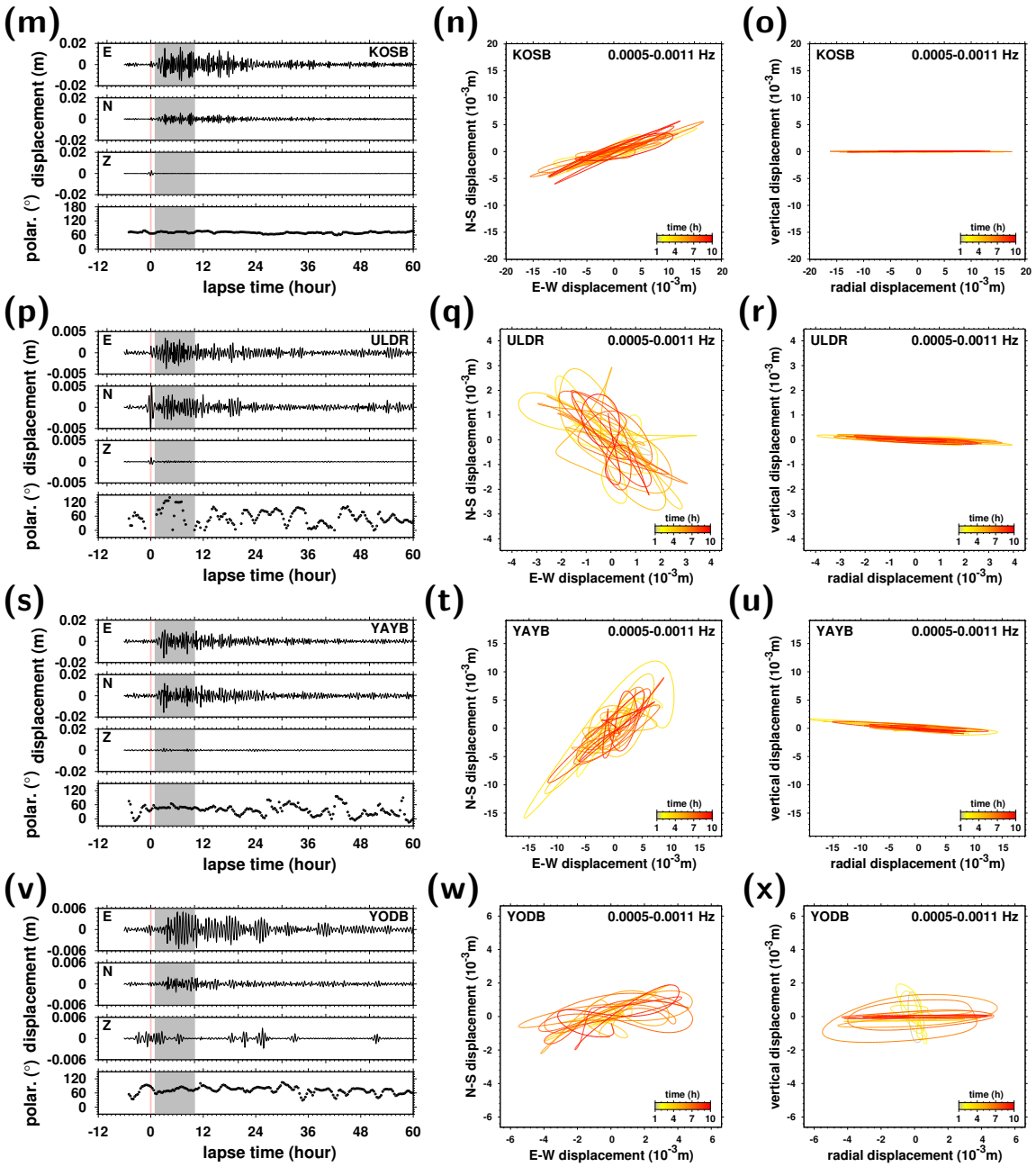


**Figure S6.** *(continued)*

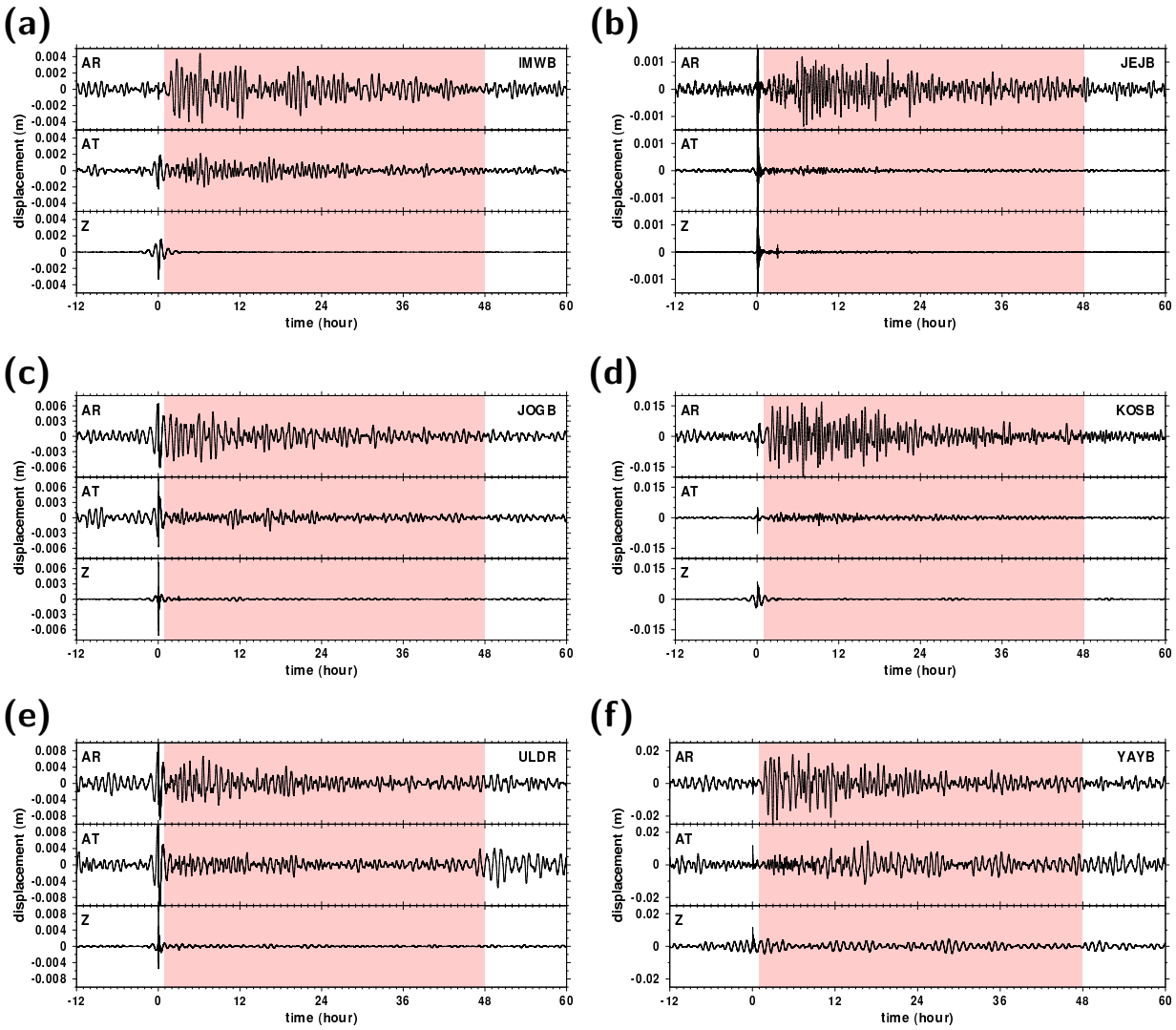


**Figure S7.** Rotated tsunami-induced seismic signals in frequencies of 0.0003-0.01 Hz at stations (a) IMWB, (b) JEJB, (c) JOGB, (d) KOSB, (e) ULDR, and (f) YAYB. The tsunami-induced seismic signals are strong in the apparent radial directions.

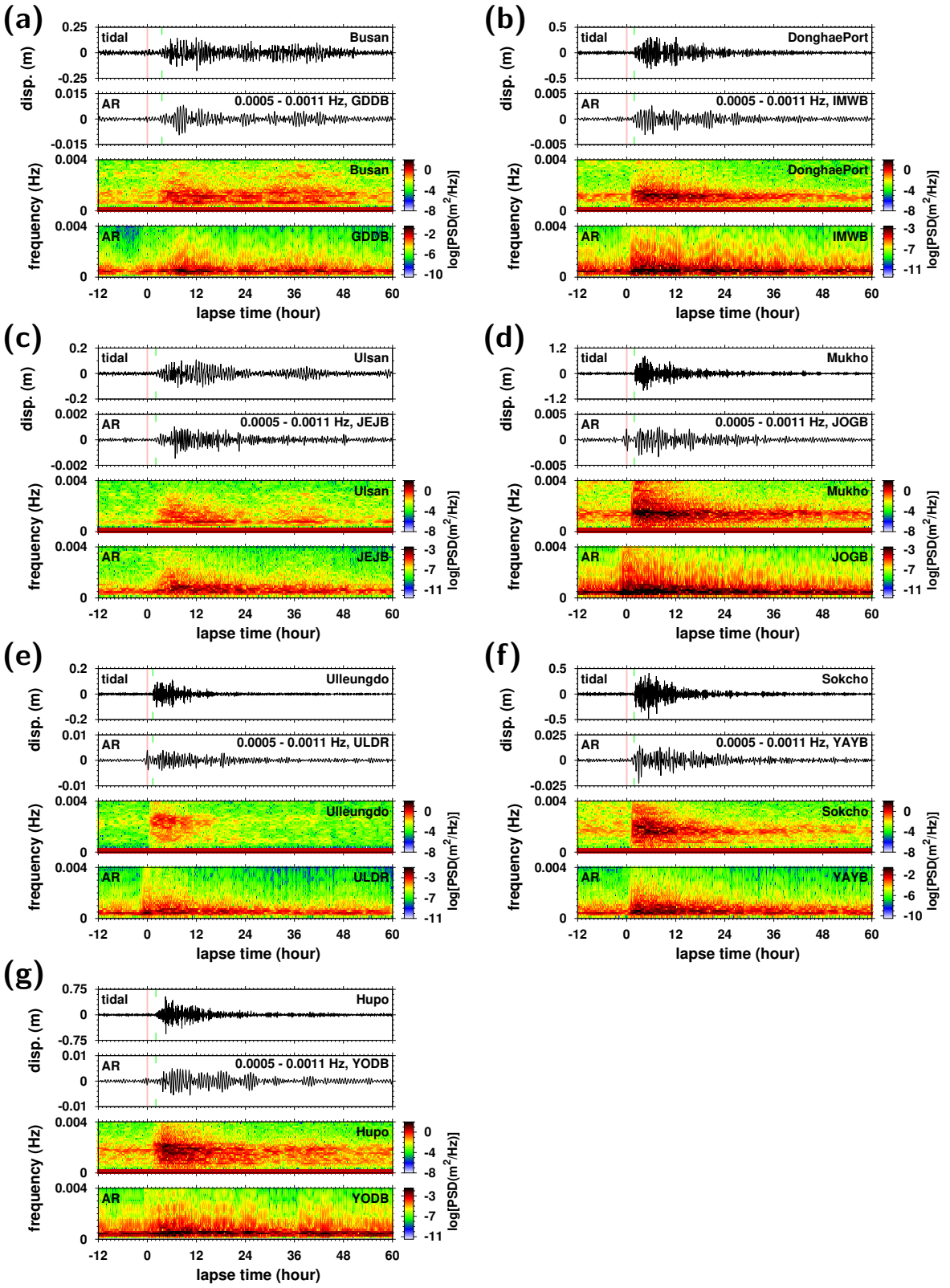


**Figure S8.** Comparison of waveforms and spectral contents between tsunami records in tide gauges and tsunami-induced seismic signals in adjacent seismic stations: seismic stations (a) GDDB, (b) IMWB, (c) JEJB, (d) JOGB, (e) ULDR, (f) YAYB, and (g) YODB. The waveforms and spectral contents are similar between tide gauges and seismic stations.

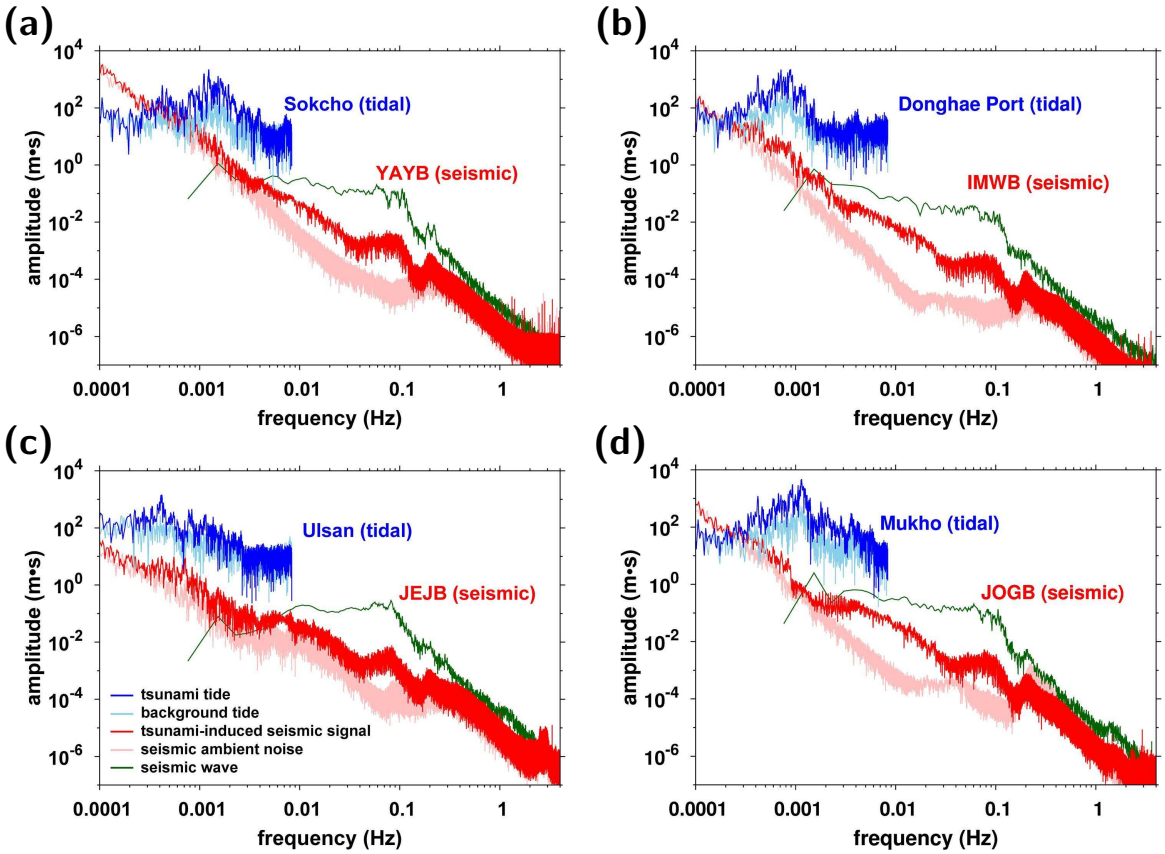


**Figure S9.** Comparison of spectral amplitudes between tsunami records in tide gauges and tsunami-induced seismic signals at adjacent seismic stations (a) YAYB, (b) IMWB, (c) JEJB, and (d) JOGB. The spectral contents of seismic waves from the earthquakes are additionally presented.

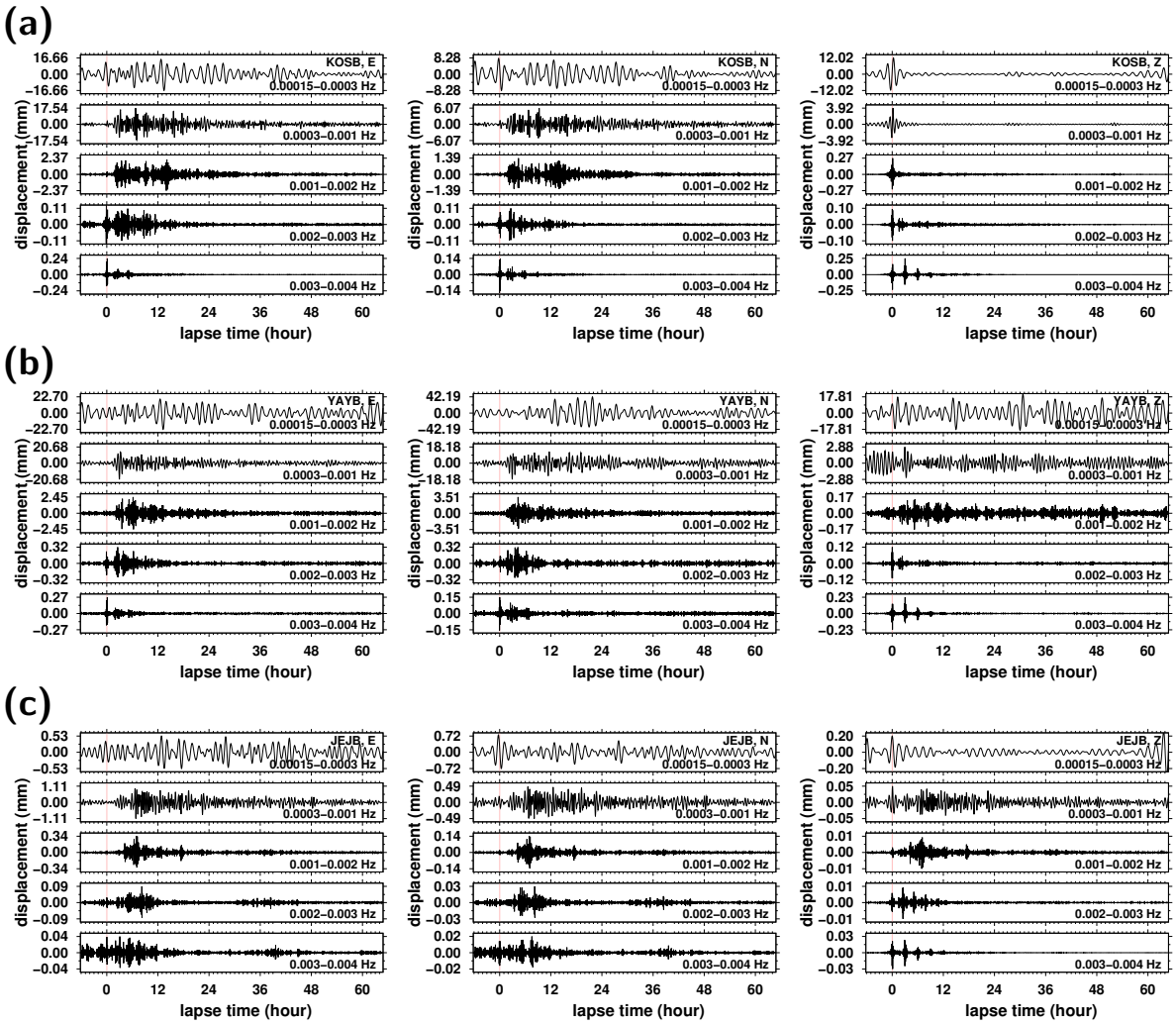


**Figure S10.** Three-component (EW, NS, and vertical) bandpass-filtered record sections for 65 hours after the event origin time at stations (a) KOSB, (b) YAYB, and (c) JEJB. The tsunami-induced seismic signals are effectively observed in frequencies less than 0.002 Hz. Reflected body waves and surface waves around the Earth appear in higher frequencies ($> 0.002$ Hz).

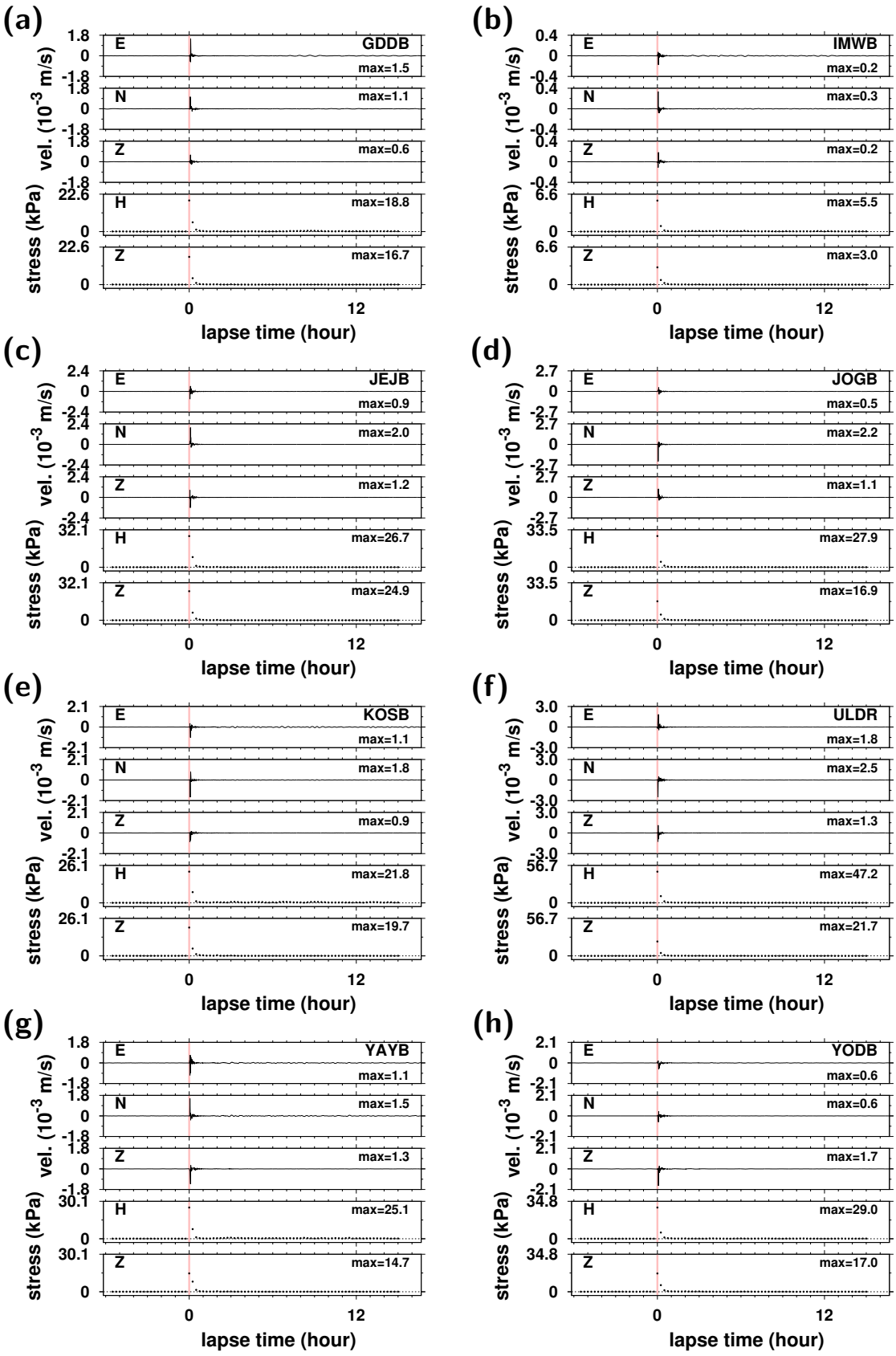


**Figure S11.** Dynamic stress changes induced by seismic waves at stations (a) GDDB, (b) IMWB, (c) JEJB, (d) JOGB, (e) KOSB, (f) ULDR, (g) YAYB, and (h) YODB.

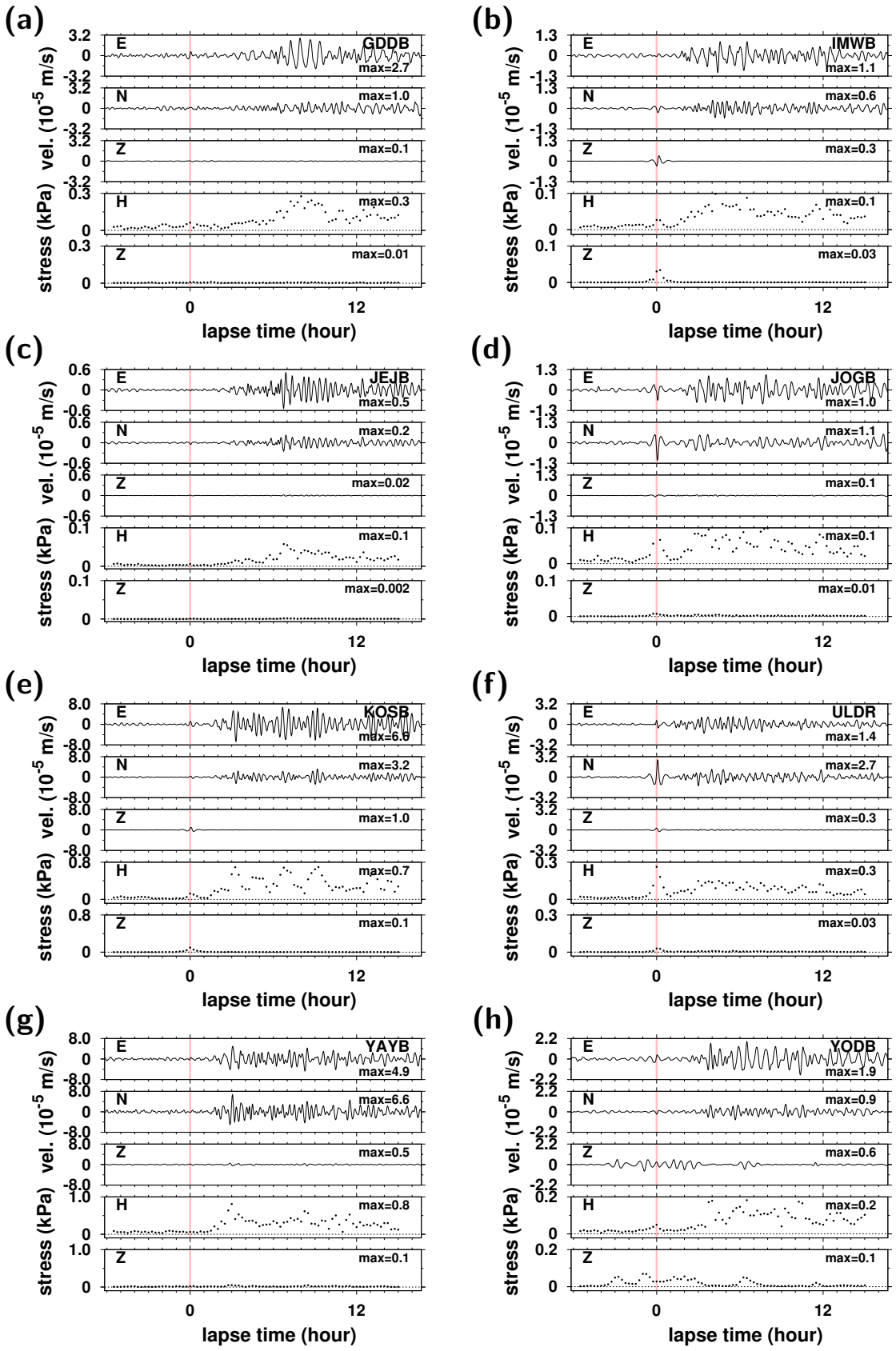


**Figure S12.** Dynamic stress changes caused by tsunami-induced seismic signals recorded at stations (a) GDDB, (b) IMWB, (c) JEJB, (d) JOGB, (e) KOSB, (f) ULDR, (g) YAYB, and (h) YODB.

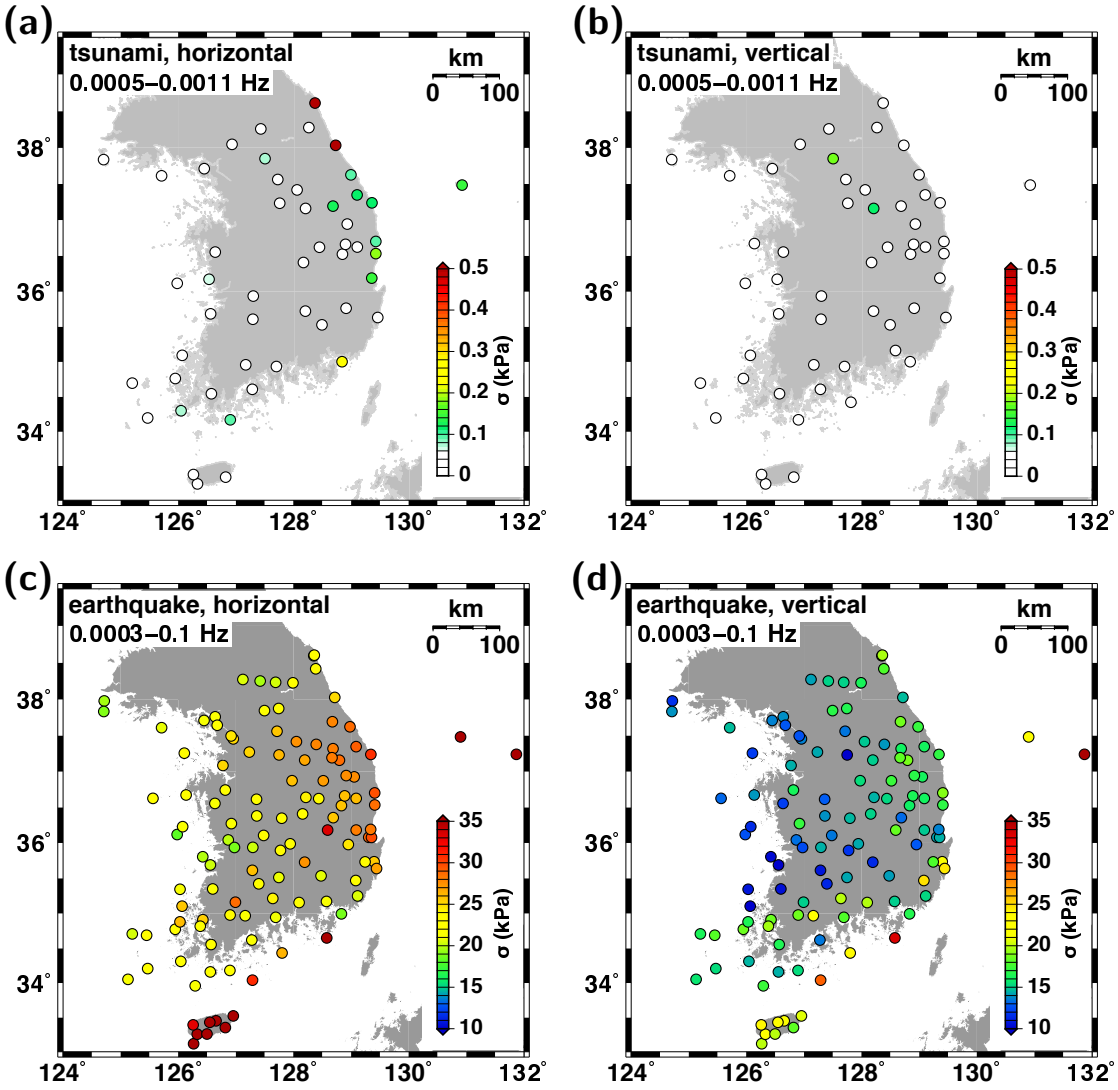


**Figure S13.** Spatial variations in peak dynamic stress changes by tsunami-induced signal in frequencies of 0.0005-0.0011 Hz in (a) horizontal and (b) vertical directions, and those by seismic wavetrains in frequencies of 0.0003-0.1 Hz in (c) horizontal and (d) vertical directions. The strengths of tsunami-induced seismic signals are relatively large along the east coast. The peak dynamic stress change by the seismic wavetrains generally decreases with distance from the earthquake.

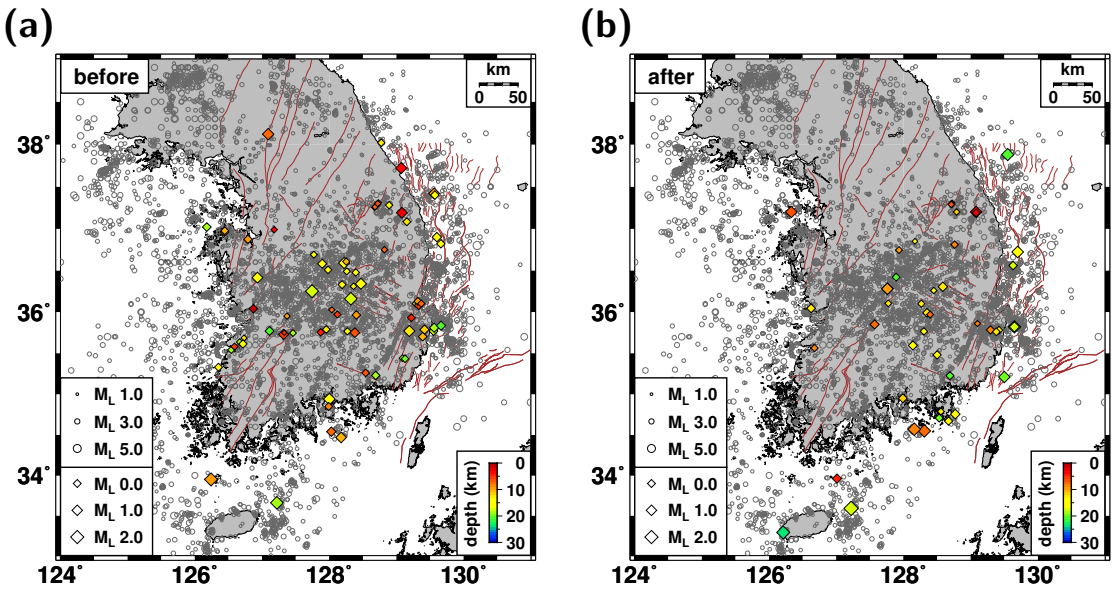


**Figure S14.** Seismicity in the Korean Peninsula (a) before and (b) after the earthquake. The seismicity presents no apparent changes after the earthquake.